Published for SISSA by Springer

Received: February 16, 2019
Revised: May 9, 2019
Accepted: June 7, 2019
Published: June 20, 2019

Two-mediator dark matter models and cosmic electron excess

Xuewen Liu,[a] **Zuowei Liu**[a,b,c] **and Yushan Su**[a]

[a] *Department of Physics, Nanjing University, Nanjing 210093, China*
[b] *Center for High Energy Physics, Peking University, Beijing 100871, China*
[c] *CAS Center for Excellence in Particle Physics, Beijing 100049, China*

E-mail: xuewenliu@nju.edu.cn, zuoweiliu@nju.edu.cn, 151150045@smail.nju.edu.cn

Abstract: The cosmic electron energy spectrum recently observed by the DAMPE experiment exhibits two interesting features, including a break around 0.9 TeV and a sharp resonance near 1.4 TeV. In this analysis, we propose a dark matter explanation to both exotic features seen by DAMPE. In our model, dark matter annihilates in the galaxy via two different channels that lead to both a narrow resonance spectrum near 1.4 TeV and electron excess events over an extended energy range thus generating the break structure around TeV. The two annihilation channels are mediated by two gauge bosons that interact both with dark matter and with the standard model fermions. Dark matter annihilations through the s-channel process mediated by the heavier boson produce monoenergetic electron-positron pairs leading to the resonance excess. The lighter boson has a mass smaller than the dark matter such that they can be on-shell produced in dark matter annihilations in the galaxy; the lighter bosons in the final state subsequently decay to generate the extended excess events due to the smeared electron energy spectrum in this process. We further analyze constraints from various experiments, including HESS, Fermi, AMS, and LHC, to the parameter space of the model where both excess events can be accounted for. In order to interpret the two new features in the DAMPE data, dark matter annihilation cross sections in the current galaxy are typically much larger than the canonical thermal cross section needed for the correct dark matter relic abundance. This discrepancy, however, is remedied by the nonperturbative Sommerfeld enhancement because of the existence of a lighter mediator in the model.

Keywords: Beyond Standard Model, Cosmology of Theories beyond the SM

ArXiv ePrint: 1902.04916

https://doi.org/10.1007/JHEP06(2019)109

JHEP06(2019)109

Contents

JHEP06(2019)109

1 Introduction

Recently, DAMPE collaboration reported new measurements of the cosmic electron flux, which exhibit two exotic features in the energy spectrum, including a so-called break structure around 0.9 TeV and a sharp resonance near 1.4 TeV [1]. The morphology of the excess electron events near 1.4 TeV in the DAMPE data hints a nearby cosmic ray source; a number of papers have appeared to interpret the DAMPE narrow resonance near 1.4 TeV, including astrophysical sources [2–5] and dark matter (DM) sources [4–41].[1] So far, most papers interpret only the 1.4 TeV excess as signals of a local source. In this analysis, we argue that both the 0.9 TeV break and the 1.4 TeV resonance in the DAMPE electron spectrum could have a common origin.

We propose a dark matter explanation to both the break and the resonance in the DAMPE electron data. A dark matter subhalo (SH) is assumed to exist in the vicinity of the solar system motivated by the morphology of the 1.4 TeV resonance excess. We assume a simple cosmic electron background, a single power-law form with only two parameters. Thus, both the break and the sharp resonance in the DAMPE data have emerged as results of excess electrons in dark matter annihilations in the nearby subhalo.

We propose a two-mediator dark matter model (2MDM) to interpret the excess electrons seen by DAMPE. In our model, dark matter can annihilate in the galaxy via two different annihilation channels due to the two mediators that interact both with dark matter and with the standard model (SM) sector. The two annihilation channels produce distinct signatures in cosmic electron flux because of different mass hierarchies between DM and mediators. One of the two mediators, denoted as V_1, has a mass nearly twice of the DM particle; thus the dominated annihilation channel mediated by the V_1 boson is the $\chi\bar{\chi} \to V_1 \to e^- e^+$ process which produces cosmic electrons (and positrons) with energy equal to the DM mass. This then leads to a sharp resonance in the energy spectrum, when DM annihilates in a nearby subhalo. Because the sharp resonance in the DAMPE data occurs around 1.4 TeV, we take the DM mass to be 1.5 TeV.

The other mediator, denoted by V_2, is much lighter than DM such that the pair-production of on-shell V_2 bosons ($\chi\bar{\chi} \to V_2 V_2$) becomes the primary DM annihilation channel among the processes mediated by the V_2 boson. The lighter mediator V_2 in the final state further decays to produce SM fermions. If the V_2 boson can directly decay into a pair of electron and positron, the electrons (and positrons) have a box-shape energy spectrum which is centered at one-half of the DM mass and has a width determined by the mass ratio between V_2 and DM. The box-shape electron energy spectrum is further altered during the propagation between the source (the DM subhalo) and the observation point (the DAMPE satellite) to generate an extended excess in the electron energy spectrum. This then gives rise to a "break" structure roughly at one-half of the DM mass (~ 750 GeV in our case) in the electron energy spectrum observed by DAMPE. In our model, because the V_2 boson is $L_\mu - L_\tau$ gauged so that the electrons originating from V_2 decays only carry a fraction of the total energy, the electron energy spectrum is further smeared.

[1] see e.g. [42] for the significance analysis of the excess.

JHEP06(2019)109

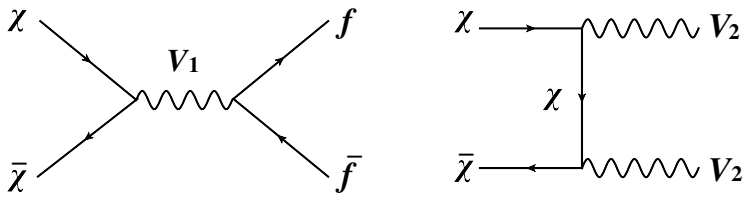

Figure 1. Feynman diagrams for the two different annihilation channels with different mediators.

Thus, both the break and the sharp resonance observed by DAMPE arise due to the electrons coming from DM annihilations in the 2MDM model. We begin in section 2 by presenting the two-mediator DM models in which DM interacts with SM via two different gauge bosons. In section 3, we provide the cosmic electron background used in the analysis. In section 4, we describe the method to compute electron flux from DM annihilations both in the DM subhalo and in the Milky Way (MW) halo, as well as the method to compare our calculations with DAMPE data. In section 5, we compute the DAMPE signals expected in the two-mediator dark matter models. In section 6, we analyze HESS constraints on our DM model. In section 7, we study the constraints from the Fermi isotropic gamma ray background measurements. In section 8, we investigate AMS constraints on our DM model. In section 9, we calculate ATLAS constraints on our DM model. In section 10, we discuss Sommerfeld enhancement in our model and the impacts on DM relic abundance. In section 11, we summarize our findings.

2 The two-mediator dark matter model

We consider DM models in which DM is a Dirac fermion and charged under two U(1) fields; the corresponding gauge bosons are V_1 and V_2. Hinted by the sharp resonance near 1.4 TeV in the DAMPE data, we fix the DM mass at 1.5 TeV. The mass of the V_1 boson can be near 3 TeV; The mass of the V_2 is lighter than the DM mass such that V_2 can be on-shell produced in DM annihilations in the DM halo. Thus the relevant DM annihilation channels are

$$\chi\bar{\chi} \to V_1 \to f\bar{f} \tag{2.1}$$

$$\chi\bar{\chi} \to V_2 V_2 \to f\bar{f}f'\bar{f}' \tag{2.2}$$

The Feynman diagrams for the two annihilation channels are shown in figure 1.

In our analysis, we consider two cases: (1) V_1 is electrophilic and V_2 is the $L_\mu - L_\tau$ gauged; (2) V_1 is hidden and kinetically mixes with the SM hypercharge and V_2 is $L_\mu - L_\tau$ gauged. Below we provide one concrete model in the latter case where a Dirac fermion dark matter particle χ couples to two spin-1 mediators V_1 and V_2:

$$\begin{aligned}\mathcal{L} \supset & -\frac{1}{4}V_1^{\mu\nu}V_{1\mu\nu} + g_1\bar{\chi}\gamma_\mu\chi V_1^\mu + \frac{\epsilon}{2}V_1^{\mu\nu}B_{\mu\nu} - \frac{1}{4}V_2^{\mu\nu}V_{2\mu\nu} + g_2\bar{\chi}\gamma_\mu\chi V_2^\mu \\ & + g_2(\bar{\mu}\gamma_\mu\mu - \bar{\tau}\gamma_\mu\tau + \bar{\nu}_\mu\gamma_\mu P_L\nu_\mu - \bar{\nu}_\tau\gamma_\mu P_L\nu_\tau)V_2^\mu,\end{aligned} \tag{2.3}$$

JHEP06(2019)109

where ϵ is the kinetic mixing parameter between gauge boson $V_{1\mu}$ and the SM U(1)$_Y$ hypercharge gauge boson B_μ, $g_1(g_2)$ is the gauge coupling for bosons $V_{1\mu}$ ($V_{2\mu}$). Here DM fields carry the $L_\mu - L_\tau$ quantum number. $V_{1\mu\nu}(V_{2\mu\nu})$ is the field strength of $V_{1\mu}$ ($V_{2\mu}$); $B_{\mu\nu}$ is the SM U(1)$_Y$ field strength. For the first case in which V_1 is electrophilic, in general one could substitute the kinetic mixing term in the above Lagrangian with $V_1^\mu \bar{e}\gamma_\mu(v_e - a_e\gamma_5)e$ to mediate the interaction between the V_1 boson and electron.

3 Cosmic electron background

Because DAMPE does not distinguish the charge of electron/positron events, we assume the following single power-law background (BG) for the total flux of electron and positron,

$$\Phi_{e^\pm}^{\rm BG} = CE^{-\gamma}, \tag{3.1}$$

where C and γ are free parameters to be determined by data. The simple power-law background is motivated by the Fermi mechanism.[2] In our analysis, we use the first eight points and the last eight points in the DAMPE data [1] to fit this single power-law background, and obtain the following best-fit parameters: $C = 458$ (GeV m^2 s sr)$^{-1}$ and $\gamma = 3.25$.[3] We use these background parameters throughout our study. Since DAMPE is unable to discriminate electrons from positrons, we will use the word "electron" in this paper to collectively denote both electron and positron when there is no confusion.

4 Electron flux from DM annihilations

The sharp resonance of the excess events near 1.4 TeV in the DAMPE data hits a nearby electron/positron source. To fit the spectrum of the DAMPE data, we introduce a nearby DM subhalo with the generalized NFW profile [43–45]

$$\rho(r) = \rho_s \frac{(r/r_s)^{-\gamma}}{(1 + r/r_s)^{3-\gamma}}. \tag{4.1}$$

We use the following parameters for the subhalo: $\gamma = 0.5$, $\rho_s = 100$ GeV/cm^3, and $r_s = 0.1$ kpc [6]. The distance between the subhalo and us (denoted by d_s) is also crucial to the cosmic ray spectrum. We find that the above subhalo with $d_s = 0.3$ kpc can fit the DAMPE data well. The above values of the four parameters are assumed for the subhalo in our analysis if not specified otherwise.

The electron/positron flux can originate from dark matter annihilations both in the Milky Way dark matter halo and in a nearby subhalo. The electron flux from DM annihilations in the MW halo (denoted by $\Phi^{\chi-{\rm MW}}$) is computed via PPPC4DMID [46]. For

[2] Although more complicated cosmic backgrounds with exponential breaks have been used in the literature to fit the cosmic electron flux, it remains unclear if the propagation of the cosmic rays in the Milky Way galaxy can actually give rise to such background models. In order to explore the possibility of generating the break feature in DAMPE via DM annihilations, we thus assume a simple power-law background in our analysis.

[3] Alternative methods of obtaining the parameters in the background are discussed later in section 5.1.

JHEP06(2019)109

the electron flux arising from DM annihilations in a nearby subhalo, we use the Green's function method [6, 47–49]

$$\Phi^{\chi-\mathrm{SH}}(\mathbf{x}, E) = \frac{v_e}{4\pi} \int d^3x_s \int dE_s \, G(\mathbf{x}, E; \mathbf{x}_s, E_s) Q(\mathbf{x}_s, E_s), \tag{4.2}$$

where $G(\mathbf{x}, E; \mathbf{x}_s, E_s)$ is the Green's function, $Q(\mathbf{x}_s, E_s)$ is the source term due to DM annihilation, v_e is the electron velocity, and $\Phi^{\chi-\mathrm{SH}}(\mathbf{x}, E)$ is the electron flux due to DM annihilations in the subhalo, which has the unit of (GeV^{-1} m^{-2} s^{-1} sr^{-1}). Here the subscript s indicates the quantities associated with the DM source. The Green's function can be calculated via $G(\mathbf{x}, E; \mathbf{x}_s, E_s) = b(E)^{-1}(\pi\lambda^2)^{-3/2} \exp\left[-(\mathbf{x}-\mathbf{x}_s)^2/\lambda^2\right]$ with the propagation scale λ being given by $\lambda^2 = 4\int_E^{E_s} dE' D(E')/b(E')$ where the energy loss coefficient $b(E) = b_0(E/\mathrm{GeV})^2$ with $b_0 = 10^{-16}\,\mathrm{GeV/s}$ and the diffusion coefficient $D(E) = D_0(E/\mathrm{GeV})^\delta$ with $D_0 = 11\,\mathrm{pc}^2/\mathrm{kyr}$, and $\delta = 0.7$ [50]. The source function due to DM annihilations is

$$Q(\mathbf{x_s}, E_s) = \frac{1}{4}\frac{\rho_\chi^2(\mathbf{x_s})}{m_\chi^2}\langle\sigma v\rangle\frac{dN}{dE_s}(E_s), \tag{4.3}$$

where m_χ is the DM mass, $\rho_\chi(\mathbf{x_s})$ is the DM mass density, $\langle\sigma v\rangle$ is the velocity-averaged DM annihilation cross section, dN/dE_s is the electron energy spectrum per DM annihilation.

Thus, in our analysis, the total electron flux is given by $\Phi^{\mathrm{th}} = \Phi^{\mathrm{BG}} + \Phi^{\chi-\mathrm{MW}} + \Phi^{\chi-\mathrm{SH}}$ where we consider three major contributions: the cosmic ray background, DM annihilations in the MW halo, and DM annihilations in the nearby subhalo. To compare our calculations with the DAMPE data, we further take into account the "bin effects" by performing the following computation

$$\Phi_i^{\mathrm{th}} = \frac{1}{E_i^{\mathrm{max}} - E_i^{\mathrm{min}}} \int_{E_i^{\mathrm{min}}}^{E_i^{\mathrm{max}}} \Phi^{\mathrm{th}}(E) dE, \tag{4.4}$$

where E_i^{min} (E_i^{max}) is the lower (upper) bound of the i-th bin in the DAMPE data. To fit the DAMPE data, we carry out the following χ^2 analysis

$$\chi^2 = \sum_i \frac{(\Phi_i^{\mathrm{th}} - \Phi_i^{\mathrm{exp}})^2}{\delta_i^2}, \tag{4.5}$$

where Φ_i^{exp} (δ_i) is the electron flux (uncertainty) reported by the DAMPE experiment [1].

5 DAMPE excess events in the two-mediator dark matter models

In this section, we compute the electron flux expected in DAMPE from DM annihilations in the two-mediator DM model. DM annihilations both in the subhalo and in the MW halo are considered in our analysis. We use $\langle\sigma v\rangle_1$ to denote the velocity averaged DM annihilation cross section for the $\chi\bar{\chi} \to V_1 \to f\bar{f}$ process, which is mediated by the heavier gauge boson V_1; we use $\langle\sigma v\rangle_2$ to denote the velocity averaged DM annihilation cross section for the $\chi\bar{\chi} \to V_2V_2$ process where the lighter gauge boson V_2 is on-shell produced. The annihilation cross sections $\langle\sigma v\rangle_1$ and $\langle\sigma v\rangle_2$ are mainly responsible for the resonance and the break excess events in the DAMPE electron spectrum respectively.

JHEP06(2019)109

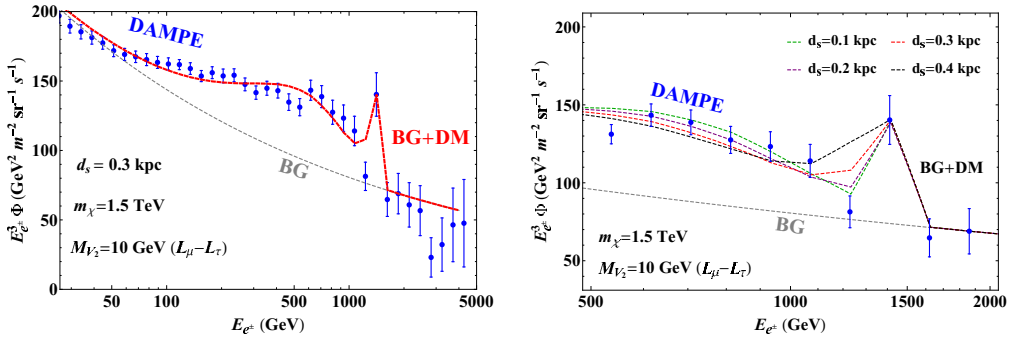

Figure 2. Left panel: DAMPE electron energy spectrum. Overlaid is the sum of cosmic ray background and the electron flux from DM annihilations from the MW halo and from the nearby subhalo, which is $d_s = 0.3\,\text{kpc}$ away from us. Right panel: same as the left panel except that we take different d_s values: $d_s = 0.1, 0.2, 0.3, 0.4\,\text{kpc}$. Here V_1 is electrophilic and V_2 is $L_\mu - L_\tau$ gauged.

5.1 Electrophilic and gauged $L_\mu - L_\tau$

Here we first consider the two-mediator model in which the heavier mediator V_1 is electrophilic and the lighter mediator V_2 is the $L_\mu - L_\tau$ gauge boson. In this case, for the annihilation process mediated by the V_1, only $\chi\bar{\chi} \to V_1 \to e^+e^-$ can occur. In the annihilation processes where V_2 is on-shell produced, V_2 further decays into $\mu\mu$, $\tau\tau$, and $\nu\nu$ final states with branching ratio BR = 1/3 for each final state. The energy spectrum of the $\mu\mu$ and $\tau\tau$ final states exhibits a box-like distribution that is centered at $m_\chi/2$ (see e.g. [51–56] for early studies in the context of cosmic rays). In our analysis, because we assume a simple power-law background, there is a wide range of electron excess events, extending from about 50 GeV to almost over 1 TeV, as shown in the left panel figure of figure 2. To generate such an extended electron excess events, the mass of the V_2 boson has to be sufficiently small since the width of the box-shape energy spectrum is given by $\sqrt{m_\chi^2 - m_{V_2}^2}$. In addition, the V_2 boson in our study is also required to decay into the $\tau\tau$ final state. Thus we take 10 GeV as the benchmark point for the V_2 boson mass, which is assumed throughout our analysis.

The left panel figure of figure 2 shows the DAMPE electron flux data, the cosmic ray background, and the electron flux from both DM annihilations and background, where the subhalo takes its default parameters. Here the 1.4 TeV peak shown in figure 2 mainly comes from the $\chi\bar{\chi} \to V_1 \to e^-e^+$ annihilation channel; the 0.9 TeV break shown in figure 2 is primarily due to the $\chi\bar{\chi} \to V_2V_2$ annihilation channel. The formation of the break structure in the electron energy spectrum here is due to several aspects of the problem here. Because the mass of V_2 in our analysis is taken to be 10 GeV, the box-shape energy spectrum of $\mu\mu$ and $\tau\tau$ have a wide energy range (extending almost from zero to $2m_\chi$). The energy loss in charged lepton decays and cosmic ray propagation in addition shapes the excess electrons. Thus one obtains an extended distribution of the excess electrons with a power-law break around TeV.

JHEP06(2019)109

d_s (kpc)	0.1	0.2	0.3	0.4
$\sigma v(\chi\bar{\chi} \to e^+e^-)(\mathrm{cm}^3/\mathrm{s})$	7.9×10^{-27}	2.1×10^{-26}	4.9×10^{-26}	1.1×10^{-25}
$\sigma v(\chi\bar{\chi} \to V_2V_2)$ $(\mathrm{cm}^3/\mathrm{s})$	6.5×10^{-25}	1.3×10^{-24}	2.0×10^{-24}	2.8×10^{-24}

Table 1. Best-fitted cross sections of the $\chi\bar{\chi} \to e^+e^-$ and $\chi\bar{\chi} \to V_2V_2$ processes for different d_s values. Here V_2 is the $L_\mu - L_\tau$ gauge boson.

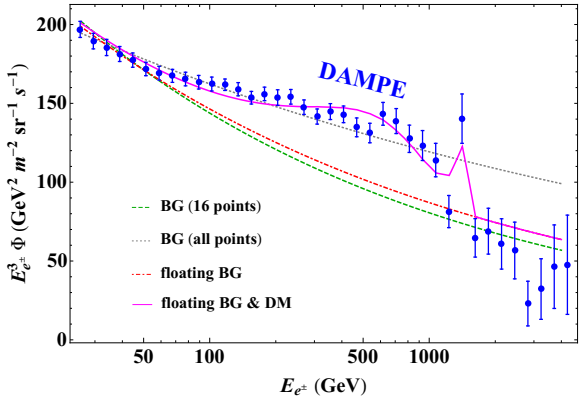

Figure 3. Fitting the DAMPE data with different hypotheses. A subhalo is assumed to be 0.3 kpc away from us. The green line (dashed) is the best-fit background obtained by fitting the first eight and last eight DAMPE data points. The gray line (dotted) is the best-fit background obtained by fitting all the DAMPE data points. The magenta line (solid) is the best-fit electron flux when one fits the DAMPE data with the sum of a floating background and DM contributions. The red line (dot-dashed) indicates the background component of the magenta line.

We further vary the distance between the subhalo and us on the right panel figure of figure 2, while keeping the rest of the parameters fixed for the subhalo. For each d_s value, we find the best-fit DM annihilation cross sections for both channels in fitting the DAMPE data, which are shown in table 1. We will adopt the case in which $d_s = 0.3\,\mathrm{kpc}$ as the benchmark model for our analysis, in which the DM annihilation cross sections for the two channels take $\langle\sigma v\rangle_1 = 4.9\times10^{-26}\,\mathrm{cm}^3/\mathrm{s}$ and $\langle\sigma v\rangle_2 = 2.0\times10^{-24}\,\mathrm{cm}^3/\mathrm{s}$. Taking into account the Sommerfeld enhancement effects (see section 10 for the detailed discussions), we find that one should have $g_2 = 0.68$ in order to obtain $\sigma v(\chi\bar{\chi} \to V_2V_2) = 2.0 \times 10^{-24}\,\mathrm{cm}^3/\mathrm{s}$.

So far, we have held the cosmic background fixed in fitting the DAMPE data, which we referred to as the "fixed BG" method. Below we perform the analysis letting the parameters in the cosmic background vary, which we referred to as the "floating BG" method.

In figure 3, we fit the DAMPE data with different hypotheses. The total χ^2 is 136 when one fits all DAMPE data with the cosmic electron background given by eq. (3.1); the best-fit values for the cosmic background are: $C = 301$ (GeV m^2 s sr)$^{-1}$ and $\gamma = 3.13$. The total χ^2 reduces to 54 when one fits all DAMPE data with the floating BG plus DM contributions; the best-fit values are: $C = 415$ (GeV m^2 s sr)$^{-1}$, $\gamma = 3.23$, $\langle\sigma v\rangle_1 = 3.1 \times 10^{-26}\,\mathrm{cm}^3/\mathrm{s}$ (the electrophilic V_1 channel), and $\langle\sigma v\rangle_2 = 1.9 \times 10^{-24}\,\mathrm{cm}^3/\mathrm{s}$ (the $L_\mu - L_\tau$ V_2 channel). There is a clear indication that the DAMPE data contain exotic features that cannot be

JHEP06(2019)109

described by the simple power-law background. For the fixed BG method, we have $\chi^2 = 62$ for the best-fit cross sections given in table 1 (the 0.3 kpc case). The difference between the best-fit floating BG and the fixed BG is negligible as shown in figure 3: The floating BG provides an almost identical flux in the low energy regime as the fixed BG; for the last eight bins in the DAMPE data, the floating BG gives a little larger fluxes than the central values of the data points. Because there is no signal from DM annihilations beyond 1.5 TeV in our model, the last eight data points in DAMPE can only originate from the background. We prefer the fixed BG method in our analysis, because it yields a better fit for the data points beyond 1.5 TeV.

5.2 Kinetic mixing and gauged $L_\mu - L_\tau$

Here we consider the two-mediator model in which the heavier mediator V_1 mixes with the SM hypercharge gauge boson via the kinetic mixing (KM) term and the lighter mediator V_2 is the $L_\mu - L_\tau$ gauge boson. The Lagrangian of this model is given in eq. (2.3). Unlike the previous case in which the V_1 is electrophilic, the annihilation process mediated by the heavier mediator $\chi\bar{\chi} \to V_1 \to f\bar{f}$ now produces all SM fermions. The analysis regarding the V_2 boson is similar to that in the previous section.

Regarding the V_1 boson in the KM case, there usually are four free parameters in the calculation: the KM parameter ϵ, the gauge coupling g_1, the DM mass m_χ which is now fixed at 1.5 TeV, and the mediator mass m_{V_1} which is typically near $2m_\chi$ to provide a sufficient annihilation rate for the DM relic abundance. However, in our case, there is another lighter mediator which can significantly change the annihilation cross section mediated by V_1 boson, via the Sommerfeld enhancement mechanism. Thus, to correctly compute the DM annihilation cross section in the halo for the $\chi\bar{\chi} \to V_1 \to f\bar{f}$ process, one has to multiply the annihilation cross section due to V_1 (see e.g. ref. [54]) and the Sommerfeld enhancement factor due to the lighter V_2 mediator (see section 10 for the detailed discussions) in the model.

In figure 4, we compute the electron flux arising from the 2MDM model in which the V_1 boson kinetically mixes with the SM hypercharge gauge boson, and the V_2 is the $L_\mu - L_\tau$ gauged boson. Here the heavier V_1 boson can decay into various SM fermions and the branching ratios are determined primarily by the hypercharge quantum numbers of the SM fermions. Since the right-handed charge lepton has a relatively large hypercharge, the total branching ratio of the V_1 boson into the three generation charge leptons is rather large, $\sum_{\ell=e,\mu,\tau} \mathrm{BR}(V_1 \to \ell^+\ell^-) \simeq 37\%$. We find that the DM annihilation cross sections $\langle\sigma v\rangle_1 = 3.9\times\ 10^{-25}\ \mathrm{cm}^3/\mathrm{s}$ (for all SM final states in the $\chi\bar{\chi} \to V_1 \to f\bar{f}$ process) and $\langle\sigma v\rangle_2 = 2.0\times\ 10^{-24}\ \mathrm{cm}^3/\mathrm{s}$ (for the $\chi\bar{\chi} \to V_2V_2$ process) provide the best fit to the DAMPE data in this model. In figure 4, the peak comes from the contributions of the $\chi\bar{\chi} \to V_1 \to f\bar{f}$ processes (mainly due to the e^+e^- final state), whereas the break are primarily due to processes mediated by the $L_\mu - L_\tau$ boson.

We note that the best-fit cross section for $\langle\sigma v\rangle_2$ is about the same as in the previous model so that $g_2 \simeq 0.68$. Taking into account the Sommerfeld enhancement factor, we find the model point $(\epsilon,\ g_1,\ m_\chi,\ M_{V_1}) = (0.01,\ 0.1,\ 1500\,\mathrm{GeV},\ 2994.2\,\mathrm{GeV})$ in the parameter space can give rise to $\langle\sigma v\rangle_1 = 3.9 \times 10^{-25}\,\mathrm{cm}^3/\mathrm{s}$. Here the mass of the V_1 boson is

JHEP06(2019)109

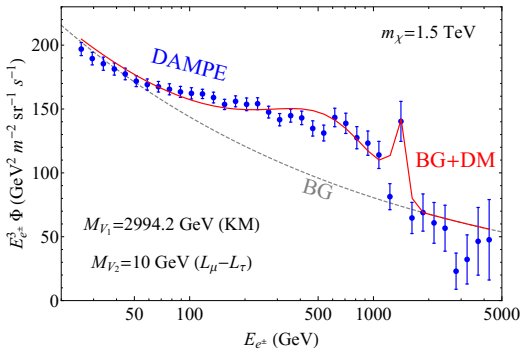

Figure 4. DAMPE electron energy spectrum. Overlaid is the sum of cosmic ray background and the electron flux from DM annihilations from the MW halo and from the nearby subhalo. Here V_1 kinetically mixes with the SM hypercharge boson and V_2 is the gauge $L_\mu - L_\tau$ boson. The DM annihilation cross sections $\langle\sigma v\rangle_1 = 3.9 \times 10^{-25}\,\mathrm{cm}^3/\mathrm{s}$ (for all SM final states in the $\chi\bar{\chi} \to V_1 \to f\bar{f}$ process) and $\langle\sigma v\rangle_2 = 2.0 \times 10^{-24}\,\mathrm{cm}^3/\mathrm{s}$ (for the $\chi\bar{\chi} \to V_2V_2$ process) are used here.

smaller than $2m_\chi$ so that the invisible decay $V_1 \to \chi\bar{\chi}$ cannot occur. In addition, the DM annihilation cross section at the early universe receives another suppression factor relative to that in the DM halo today, because the larger kinetic energy of the DM particles at the early universe moves the characteristic $\sqrt{s}$ of the DM annihilation process further away from the Breit-Wigner resonance relative to today [57]. Because the invisible decay of the V_1 boson is kinetically disallowed here and the branching ratios into charged leptons are rather significant, the discovery potential of LHC for such V_1 boson is high. The discussions on LHC constraints on this model are given in section 9.

6 HESS constraints

The gamma ray flux produced by DM annihilations can be calculated as follows

$$\frac{d\Phi_\gamma}{dE_\gamma} = \sum_i \frac{\langle\sigma v\rangle_i}{8\pi m_\chi^2} \left(\frac{dN_\gamma}{dE_\gamma}\right)_i J(\Delta\Omega), \tag{6.1}$$

where m_χ is the DM mass, $\langle\sigma v\rangle_i$ is the velocity-averaged DM annihilation cross section for channel i, $(dN_\gamma/dE_\gamma)_i$ is the gamma ray energy spectrum per annihilation for channel i, and $J(\Delta\Omega)$ is the J-factor for the region-of-interest (ROI). The differential flux $d\Phi_\gamma/dE_\gamma$ has unit of $(\mathrm{GeV\ cm^2\ s})^{-1}$. The J-factor is computed via

$$J(\Delta\Omega) = \int_{\Delta\Omega} d\Omega \int ds\, \rho_\chi^2, \tag{6.2}$$

where $\Delta\Omega$ is the solid angle of the ROI, ρ_χ is the DM density, and s is the distance along the line of light.

HESS searched for very high energy γ-rays in the inner region of the Milky Way halo, which is a circular region of 1° radius excluding a ±0.3° band in the Galactic latitude [58, 59]. With the 254-hour data accumulated [59], stringent upper bounds can be set on the DM annihilation cross sections for various SM final states. In a recent study [60],

JHEP06(2019)109

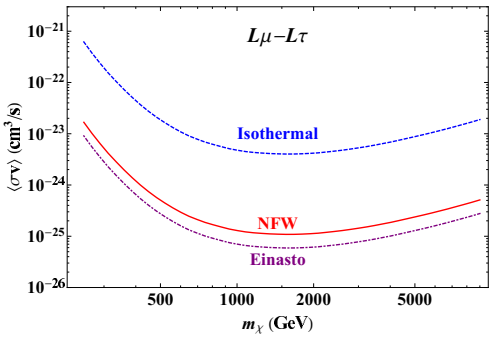

Figure 5. HESS upper limits on $\langle\sigma v\rangle(\chi\bar{\chi} \to V_2 V_2)$ where V_2 is a gauged $L_\mu - L_\tau$ boson. We considered three different DM profiles: NFW (solid), isothermal (dashed), and Einasto (dot-dashed). Here only gamma rays from the MW halo are considered. The limits are computed based on the exclusion limits for the $\chi\bar{\chi} \to \mu^+\mu^-$ and $\chi\bar{\chi} \to \tau^+\tau^-$ processes given in ref. [59]. A light V_2 mass is assumed in this analysis.

the HESS constraints on dark matter annihilations into on-shell mediators for various SM final states are analyzed. Our analysis here is similar to that in ref. [60], but in our case, on-shell mediators annihilate into a collection of SM final states with branching ratios given in the 2MDM model.

6.1 HESS constraints on DM annihilations in the Galactic center

In the following, we calculate the upper limit on the DM annihilation cross section $\langle\sigma v\rangle_{\chi\bar{\chi}\to V_2 V_2}$ from the HESS data, where V_2 is the gauge $L_\mu - L_\tau$ boson. The method we use here is to rescale the limits calculated in ref. [59] which analyzed 254-hour data recorded by HESS. The details of the method can be found in appendix B.

We first analyze the HESS limits on DM annihilations in the center of the galaxy. Because the DM distribution is not known to a good precision in the center of the galaxy and the gamma rays are very sensitive to the DM density distributions in the Galactic center, several DM profiles are considered in the HESS analyses [58, 59]. We provide a comparison of the J-factors from different DM profiles in appendix A. Here we consider three different DM profiles, NFW, Isothermal, and Einasto, to interpret the HESS constraints.

Figure 5 shows the 95% CL limits on DM annihilation cross section $\langle\sigma v\rangle_{\chi\bar{\chi}\to V_2 V_2}$ where V_2 is the gauged $L_\mu - L_\tau$ boson. For the 1.5 TeV DM annihilating into sufficiently light V_2 bosons, the HESS constraints are $\langle\sigma v\rangle_2 \lesssim 1.1 \times 10^{-25}\,(4 \times 10^{-24})$ cm^3/s for the NFW (Isothermal) profile. Thus the DM annihilation cross section $\langle\sigma v\rangle_2 = 2.0 \times 10^{-24}\,\text{cm}^3/\text{s}$ which is responsible for generating the break in the DAMPE data, is excluded if one considers the NFW or Einasto profile, but is still allowed if the isothermal profile is assumed.

6.2 HESS constraints on the location of the subhalo

DM annihilations in the subhalo also contribute to the gamma ray flux observed by the HESS experiment. Because the HESS search region is 1° around Galactic center, the gamma ray flux observed by HESS from the subhalo is a function of $l_{\rm SH}$ that is the angle

JHEP06(2019)109

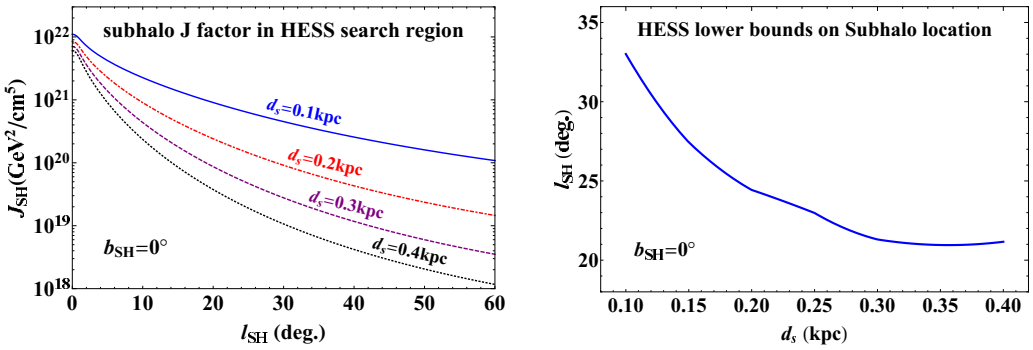

Figure 6. Left panel: the subhalo J factor in the HESS search region as the function of $l_{\rm SH}$ for different d_s values. Right panel: HESS lower limits on $l_{\rm SH}$ as a function of d_s. Here $l_{\rm SH}$ is the angle between the galactic center and the center of the subhalo.

between the Galactic center and the center of the subhalo. We compute the J factor of the subhalo inside the HESS search region in the left panel figure of figure 6 for different d_s values. The subhalo J factor increases when the subhalo moves towards either the Galactic center or us.

We further determine the minimum $l_{\rm SH}$ value by saturating the HESS constraints on DM annihilations. To determine the minimum $l_{\rm SH}$ value, we use $\langle\sigma v\rangle_{\rm DAMPE}\times(J^{\rm iso}_{\rm MW}+J_{\rm SH}(l^{\rm min}_{\rm SH}))=\langle\sigma v\rangle_{\rm HESS}\times J^{\rm iso}_{\rm MW}$, where $\langle\sigma v\rangle_{\rm DAMPE}$ is the cross section needed for the DAMPE electron excess events, as given in table 1, $J^{\rm iso}_{\rm MW}$ is the J factor inside the HESS search region for the MW halo with the isothermal DM density profile which is $7.23\times10^{19}\,{\rm GeV}^2\,{\rm cm}^{-5}$, $\langle\sigma v\rangle_{\rm HESS}$ is the HESS 95% CL upper bound on the DM annihilation cross section with the isothermal profile (which is $4\times10^{-24}\,{\rm cm}^3/{\rm s}$ as given by the isothermal curve on figure 5), $J_{\rm SH}$ is the J factor inside the HESS search region for the subhalo. Because the gamma ray flux produced by the process $\chi\bar{\chi}\to V_1\to e^+e^-$ is much smaller than $\chi\bar{\chi}\to V_2V_2$, we take $\langle\sigma v\rangle_{\rm DAMPE}\simeq\langle\sigma v\rangle(\chi\bar{\chi}\to V_2V_2)$ in the calculation here. The right panel figure of figure 6 shows the lower bound on the $l_{\rm SH}$ angle. When $d_s=0.3\,{\rm kpc}$, the subhalo has to be $>21^\circ$ away from the Galactic center to avoid HESS constraints.

6.3 HESS limits for both DM annihilation channels

Here we analyze the HESS constraints for the model in which V_1 kinetically mixes with the SM hypercharge and V_2 is $L_\mu-L_\tau$ gauged. To take both channels into consideration, we use $\Phi_\gamma(\langle\sigma v\rangle_1,m_\chi)+\Phi_\gamma(\langle\sigma v\rangle_2,m_\chi)=\Phi^{95}_\gamma(m_\chi)$, where Φ^{95}_γ is the 95% CL upper bound from the 254-h HESS data on the total gamma ray flux (in unit of ${\rm cm}^{-2}\ {\rm s}^{-1}$) integrated over the energy range $160\,{\rm GeV}<E_\gamma<m_\chi$. Here $\Phi_\gamma(\langle\sigma v\rangle_1,m_\chi)$ and $\Phi_\gamma(\langle\sigma v\rangle_2,m_\chi)$ are the gamma rays from the two annihilation channels respectively. Figure 7 shows the HESS limits for both $\langle\sigma v\rangle_1$ and $\langle\sigma v\rangle_2$ for the case where $m_\chi=1.5\,{\rm TeV}$, where only contributions from the MW halo are considered. Our model is excluded if the NFW profile is used, but allowed if the isothermal profile is used for the DM distribution in the MW halo.

JHEP06(2019)109

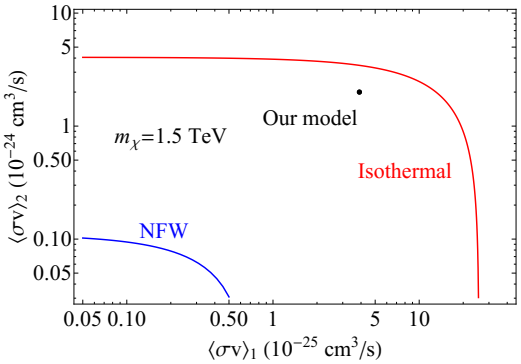

Figure 7. HESS constraints on both annihilation channels. $\langle\sigma v\rangle_1$ is the DM annihilation cross section mediated by the V_1 boson that kinetically mixes with the SM hypercharge; $\langle\sigma v\rangle_2$ is the DM annihilation cross section mediated by the V_2 boson that is $L_\mu - L_\tau$ gauged. Here $m_\chi = 1.5\,\text{TeV}$. The model point used in figure 4 is indicated by the black point here.

7 Fermi constraints

Similar to the gamma ray flux measured by HESS, the gamma ray flux observed by Fermi due to DM annihilations is calculated as follows,

$$\frac{d\Phi_\gamma}{dE_\gamma} = \sum_i \frac{\langle\sigma v\rangle_i}{8\pi m_\chi^2} \left(\frac{dN_\gamma}{dE_\gamma}\right)_i \bar{J}, \tag{7.1}$$

where $\bar{J} = J(\Delta\Omega)/\Delta\Omega$ is the J-factor averaged over the region of interest. The Fermi isotropic gamma ray background (IGRB) data are reported as an intensity flux. The gamma ray flux computed in eq. (7.1) is the intensity flux in unit of $(\text{GeV cm}^2\,\text{s sr})^{-1}$.

The isotropic gamma ray background measured by Fermi is obtained from the all-sky data excluding the $|b| < 20^\circ$ band on the Galactic plane [61]. The averaged J factor for the Fermi isotropic gamma ray background region can thus be computed as follows

$$\bar{J} = \frac{\int ds \int_{|b|>20^\circ} db\, dl \cos b\, \rho_\chi^2}{\int_{|b|>20^\circ} db\, dl \cos b}, \tag{7.2}$$

where ρ_χ is the DM density, b is the galactic latitude, ℓ is the galactic longitude, s is the distance between the point where DM annihilates and us. In this study, we take into account both the MW halo and the DM subhalo when calculating the J-factor. In this section, we consider the same isothermal DM profile for the MW halo as in the HESS analysis.

7.1 Fermi isotropic gamma ray background constraints

Here we compare the gamma ray flux produced by dark matter annihilations in the subhalo as well as in the MW halo, with the isotropic background measured by Fermi-LAT [61] to obtain constraints on our DM model. Because the galactic plane is masked in the Fermi IGRB analysis [61], the constraints from Fermi IGRB are minimized when the subhalo sits on the galactic plane. We use b_{SH} to denote the galactic latitude of the subhalo center. Thus we will set $b_{\text{SH}} = 0$ for our analysis unless specified otherwise.

JHEP06(2019)109

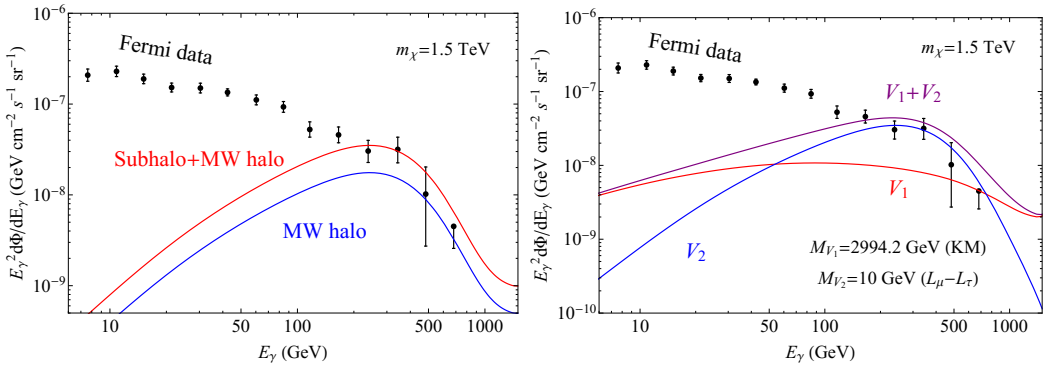

Figure 8. Left panel: Fermi IGRB data [61] and gamma rays from DM where V_1 is electrophilic and V_2 is $L_\mu - L_\tau$ gauged. Right panel: Fermi IGRB data and gamma rays from DM where V_1 is kinetically mixed with SM hypercharge and V_2 is $L_\mu - L_\tau$ gauged and has a mass of 10 GeV. DM annihilation cross sections are the same as those in figure 4. We use the default subhalo parameters for both figures.

The left panel figure in figure 8 shows the Fermi IGRB data [61] and the gamma rays from DM annihilations for the case in which the heavier V_1 boson is electrophilic and the lighter V_2 boson is $L_\mu - L_\tau$ gauged. The DM annihilation cross sections for the two annihilation channels are $(\langle\sigma v\rangle_1, \langle\sigma v\rangle_2) = (4.9 \times 10^{-26}\,\mathrm{cm}^3/\mathrm{s}, 2.0 \times 10^{-24}\,\mathrm{cm}^3/\mathrm{s})$, which are the same as those in the left panel figure of figure 2. Here the gamma ray flux arising from the $\chi\bar{\chi} \to e^+e^-$ process is only about 3% of that due to $\chi\bar{\chi} \to V_2V_2$ in this case. We find that the J-factor of the subhalo is about the same as the J-factor of the MW halo in the Fermi IGRB search region, $J_{SH} \simeq J_{MW} \simeq 6 \times 10^{21}\ \mathrm{GeV}^2/\mathrm{cm}^5$. We have plotted the gamma rays from the MW halo on the left panel figure of figure 8, as well as the gamma rays from both the MW halo and the subhalo. The predicted total gamma rays in our DM model do not exceed the current Fermi IGRB bound.

For the DM model in which the heavier V_1 boson kinetically mixes with the SM hypercharge gauge boson and the lighter V_2 boson is $L_\mu - L_\tau$ gauged, the predicted gamma rays are shown on the right panel figure in figure 8. We use the following DM annihilation cross sections $(\langle\sigma v\rangle_1, \langle\sigma v\rangle_2) = (3.9 \times 10^{-25}\,\mathrm{cm}^3/\mathrm{s}, 2.0 \times 10^{-24}\,\mathrm{cm}^3/\mathrm{s})$ which are the same as those in figure 4. Unlike the DM model presented on the left panel figure of figure 4, the annihilation process mediated by the V_1 boson on the right panel figure of figure 4 has a larger cross section and various SM final states. We plotted the gamma rays from both annihilation channels on the right panel figure of figure 4. We find that the isotropic gamma ray measurements are beginning to probe this DM model at the high energy bins in the Fermi IGRB data.

7.2 Fermi constraints on the subhalo

Here we study the effects on the Fermi IGRB data by changing various parameters for the DM subhalo. The gamma ray flux is very sensitive to the distance between the subhalo and us. We compute the gamma rays expected at Fermi using different d_s values on the left panel figure of figure 9. Different d_s values not only lead to different J-factors in the Fermi

JHEP06(2019)109

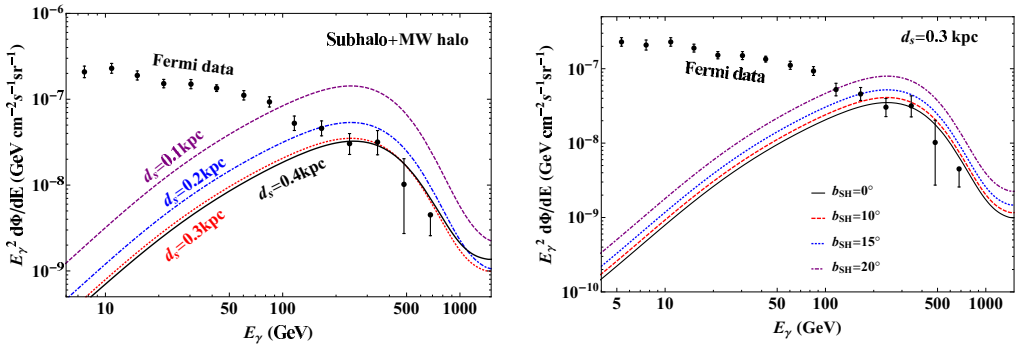

Figure 9. Left panel: Fermi IGRB data [61] and gamma rays from DM where V_1 is electrophilic and V_2 is $L_\mu - L_\tau$ gauged, with different d_s values: $d_s = (0.1, 0.2, 0.3, 0.4)$ kpc. The subhalo is placed at $b_{\rm SH} = 0°$. Right panel: same as the left panel except that we keep $d_s = 0.3\,$kpc fixed and let $b_{\rm SH}$ vary: $b_{\rm SH} = (0°, 10°, 15°, 20°)$.

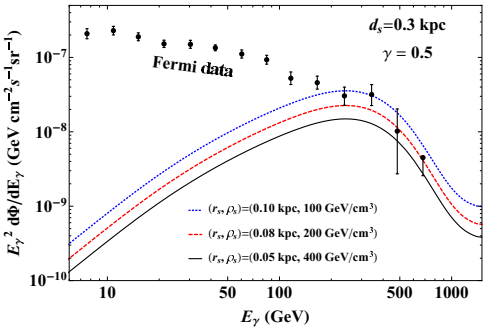

Figure 10. Fermi IGRB data [61] and gamma rays from DM for different subhalo profiles. Here V_1 is electrophilic and V_2 is $L_\mu - L_\tau$ gauged. Here $d_s = 0.3\,$kpc and $b_{\rm SH} = 0°$. The DM annihilation cross sections are $\langle\sigma v\rangle_1 = 2.33\times10^{-26}\,$cm^3/s and $\langle\sigma v\rangle_2 = 1.06\times10^{-24}\,$cm^3/s, for the case where $r_s = 0.05\,$kpc and $\rho_s = 400\,$GeV/cm^3. The DM annihilation cross sections are $\langle\sigma v\rangle_1 = 2.26\times10^{-26}\,$cm^3/s and $\langle\sigma v\rangle_2 = 1.05\times10^{-24}\,$cm^3/s, for the case where $r_s = 0.08\,$kpc, $\rho_s = 200\,$GeV/cm^3. For the case where $r_s = 0.1\,$kpc, $\rho_s = 100\,$GeV/cm^3, the DM annihilation cross sections are listed in table 1.

search region, but also lead to different DM annihilation cross sections which are provided in table 1, since one has to fit the DAMPE data. The predicted gamma rays become larger when the subhalo moves towards us. In order to evade the Fermi IGRB constraints, the subhalo has to be at least 0.3 kpc away from us. We also compute the gamma rays from the subhalo when it moves away from the Galactic plane. The gamma ray flux expected in Fermi is shown on the right panel figure of figure 9 for several different $b_{\rm SH}$ values. If the subhalo moves away from the Galactic plane for more than 10°, the gamma rays produced in the Fermi IGRB search region become significant above the current measurements.

We further study the gamma rays by changing the subhalo profile parameters (r_s, ρ_s), in the figure 10 where $d_s = 0.3\,$kpc and $\gamma = 0.5$ are fixed. Two sets of parameters in addition to the default values for the subhalo are used here. For each case, the DM annihilation cross sections for the two different channels are chosen such that one obtains the least χ^2

JHEP06(2019)109

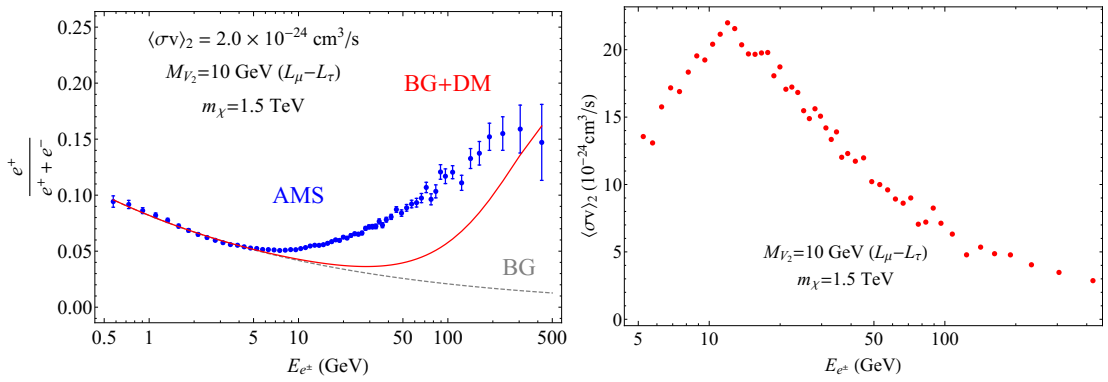

Figure 11. Left panel: AMS positron fraction data [62] and the predicted value from the $L_\mu - L_\tau$ gauge boson. Here we use $m_\chi = 1.5\,\text{TeV}$, $m_{V_2} = 10\,\text{GeV}$, and $\langle\sigma v\rangle_2 = 2.0\times\ 10^{-24}\ \text{cm}^3/\text{s}$ for the DM annihilation cross section. Right panel: 95% C.L. upper bound on $\langle\sigma v\rangle_2$ from each AMS data point.

fit to the DAMPE data. As shown in figure 10, the Fermi constraints can be significantly alleviated if the DM subhalo becomes smaller and denser.

8 AMS constraints

We do not attempt to explain the AMS positron excess, or the antiproton flux. However, the two-mediator DM model cannot produce too many positrons or antiprotons so that they violate the AMS data on the positron fraction [62] or on antiproton [63].

8.1 AMS positron constraints

To compute the AMS constraints on the DM model, we extrapolate our simple cosmic ray electron/positron background given by eq. (3.1) down to low electron energy range. We further assume that the background of the positron fraction take the following simple expression $f^{\text{BG}} = 1/(C_f E^{\gamma_f} + 1)$. We use first 15 data points in the AMS positron fraction data [62] to find the best-fit parameters: $C_f = 11.2$ and $\gamma_f = 0.31$. The positron fraction including contributions both from the background and from DM annihilations is thus computed by

$$f^{\text{th}} = \frac{\Phi^{\text{BG}} f^{\text{BG}} + \Phi^{\chi}/2}{\Phi^{\text{BG}} + \Phi^{\chi}} \tag{8.1}$$

where Φ^χ is the cosmic flux including both electron and positron due to DM annihilations. We use $(f_i^{\text{AMS}} + 1.64\,\delta f_i^{\text{AMS}})$ at each AMS data point (excluding the first 15 points) to compute the 95% C.L. upper bound on DM annihilation cross section, where f_i^{AMS} is the AMS positron fraction data and the δf_i^{AMS} is the error bar for each data point. Figure 11 shows the AMS constraints on the DM annihilation cross section mediated by the $L_\mu - L_\tau$ gauge boson using the positron fraction data. The most stringent limit comes from the highest energy bin in the AMS data, which provides the 95% CL upper bound as $\langle\sigma v\rangle_2 \lesssim 3\times10^{-24}\,\text{cm}^3/\text{s}$ for the $L_\mu - L_\tau$ gauge boson. The predicted positron fraction values at the AMS energy range in our model lie below the AMS measurements. We note in passing

JHEP06(2019)109

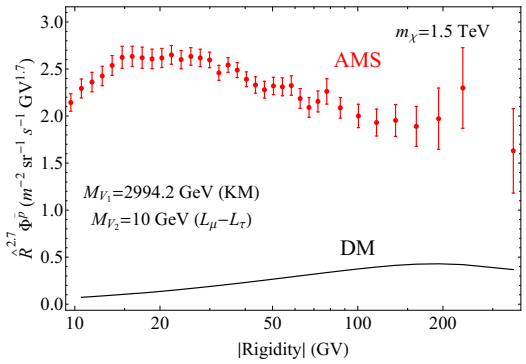

Figure 12. AMS antiproton spectrum as a function of rigidity. The red points are AMS antiproton data [63]. The black curve is the predicted antiproton flux from the DM models, where we take into account both annihilations from the MW halo and from the nearby subhalo. The subhalo profile and the DM model are the same as figure 4. The rigidity R is related to the kinetic energy T via $T = \sqrt{R^2 + m_p^2} - m_p$.

that the gap between our predicted positron fraction and the actual AMS data could be due to astrophysical sources.

8.2 AMS antiproton constraints

We compute the antiproton flux arising from the quark final states in the annihilation channel mediated by the V_1 boson that kinetically mixes with the SM hypercharge boson. The antiproton flux from DM annihilations in the MW halo is calculated via PPPC4DMID [46]; the antiproton flux from the subhalo is computed using the Green's function method, as described in appendix C. Figure 12 shows the AMS antiproton flux as a function of the rigidity R, where both the AMS data points and the theoretical predictions from our model are presented. As shown in figure 12, the antiproton flux produced by DM annihilations is far smaller than the AMS antiproton data. Therefore, we conclude that the DM model considered is allowed by the current AMS antiproton measurements.

9 LHC constraints

Here we study the LHC constraints on the V_1 boson that is kinetically mixed with the SM hypercharge. In this case, the V_1 boson couples to all SM fermions due to the kinetic mixing parameter ϵ, which is given in eq. (2.3). Thus, the V_1 boson can be produced in the Drell-Yan process at the LHC and can be searched for by reconstructing the dilepton final states. Here we utilize the recent ATLAS data [64] to put constraints on the kinetic mixing parameter ϵ between V_1 boson and the SM hypercharge boson.

Figure 13 shows the ATLAS upper bound on the dilepton production cross section, using 36.1 fb^{-1} data at the 13 TeV colliding energy. Predicted dilepton signals arising from the kinetic-mixing model and from the sequential standard model are also shown on the left panel figure of figure 13. The dilepton cross section with $\epsilon = 0.1$ for the 3 TeV $M_{Z'}$ boson in the kinetic-mixing model is below the current LHC limit. We further compute the

JHEP06(2019)109

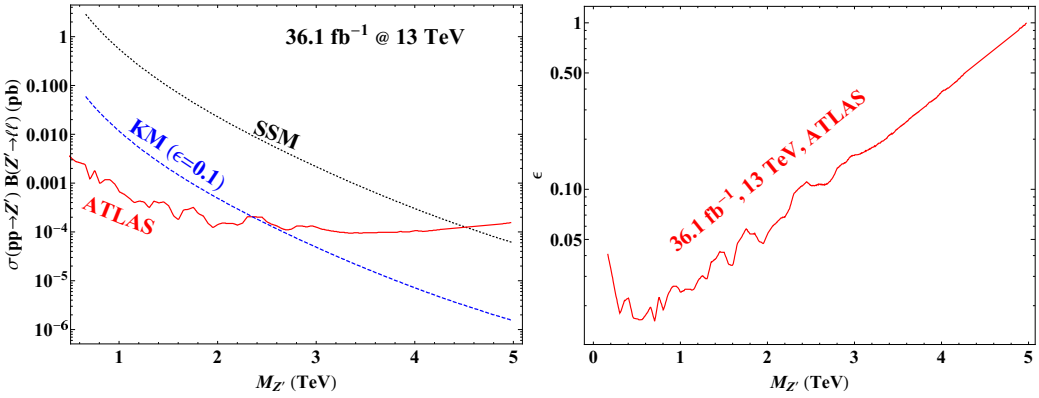

Figure 13. Left panel: ATLAS constraints (13 TeV and 36.1 fb^{-1}) [64] on the Z' boson in the dilepton channel. Overlaid are the predictions in the kinetic mixing (KM) model with parameter $\epsilon = 0.1$ and in sequential SM (SSM) model. Right panel: ATLAS upper bound on ϵ in the KM model as a function of the Z' mass.

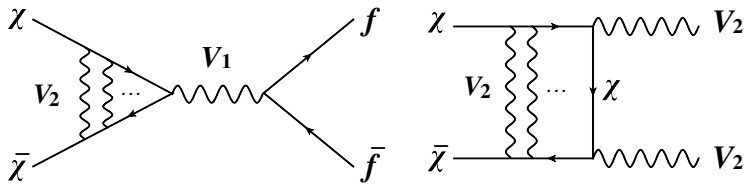

Figure 14. Illustrations of light V_2 exchanges between annihilating DM particles in the two channels which induce the Sommerfeld enhancement.

upper bound on ϵ from the dilepton final states in the entire ATLAS search range, on the right panel figure of figure 13. The limit on ϵ will certainly improve when all data currently accumulated at the LHC are analyzed (about 150 fb^{-1} data have been collected by ATLAS and by CMS individually so far [65]). However, to reach the sensitivity of probing the model point considered in our analysis, $\epsilon = 0.01$ for a 3 TeV Z' boson, more data in future LHC runs are probably needed.

10 Sommerfeld enhancement

The cross section of the process $\chi\bar{\chi} \to V_2V_2$ is larger than the canonical thermal DM annihilation cross section by about two orders of magnitude, which would suppress the DM abundance significantly. However, we should take into account the Sommerfeld enhancement induced via V_2 exchanges between DM particles in the annihilation processes as illustrated in figure 14, since the mediator V_2 is light and the velocity of DM is low in the MW halo.

The Sommerfeld enhancement factor S can be approximated by [66, 67] [56]

$$S = \left(\frac{\pi}{\epsilon_v}\right) \frac{\sinh X}{\cosh X - \cos\sqrt{(2\pi/\bar{\epsilon}_2) - X^2}}, \tag{10.1}$$

JHEP06(2019)109

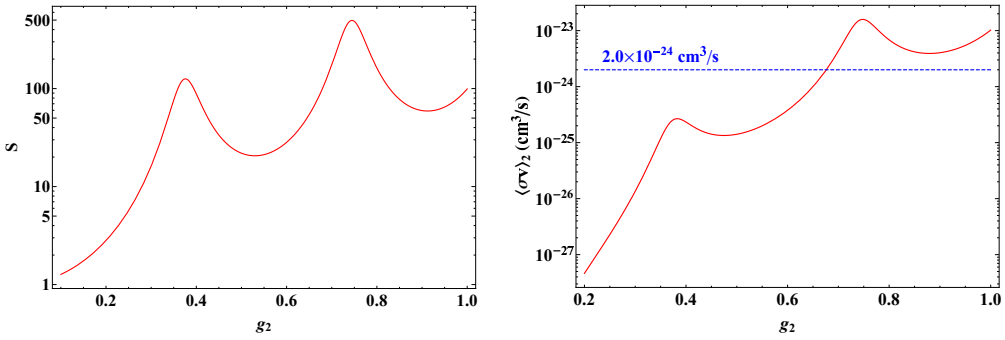

Figure 15. Left panel: Sommerfeld enhancement factor S as a function of the coupling g_2 where $m_\chi = 1.5\,\text{TeV}$ and $m_{V_2} = 10\,\text{GeV}$. Right panel: DM annihilation cross section $\langle\sigma v\rangle_2$ as a function of g_2. The blue-dashed line indicates the needed cross section to fit DAMPE data.

where $\bar{\epsilon}_2 = (\pi/12)\epsilon_2$ and $X = \epsilon_v/\bar{\epsilon}_2$, and $\epsilon_2 = m_{V_2}/(\alpha_2 m_\chi)$, $\epsilon_v = v/\alpha_2$ with $\alpha_2 = g_2^2/(4\pi)$. We take $v = 10^{-3}$ as the typical DM velocity in the halo. The left panel figure of figure 15 shows the Sommerfeld enhancement factor as a function of the gauge coupling g_2 where the mediator V_2 mass is 10 GeV and the dark matter mass is 1.5 TeV.

For the process $\chi\bar{\chi} \to V_2V_2$, the DM annihilation cross section is given by $\langle\sigma v\rangle_2 = \langle\sigma v\rangle_2^0 \times S(g_2)$ where $\langle\sigma v\rangle_2^0 \simeq g_2^4/(16\pi m_\chi^2)$ is the annihilation cross section without taking account the Sommerfeld enhancement effect. By equating this expression with $2.0 \times 10^{-24}\,\text{cm}^3/\text{s}$, the needed cross section to fit DAMPE, one obtains $g_2 = 0.68$. Thus one obtains the corresponding Sommerfeld enhancement factor $S \simeq 93$. We further plot $\langle\sigma v\rangle_2$ as a function of coupling g_2 in the right panel figure of figure 15.

For the process $\chi\bar{\chi} \to V_1 \to f\bar{f}$, one also has to consider the same enhancement due to the V_2 mediator, so that the DM annihilation cross section should be computed via $\langle\sigma v\rangle_1 = S \times \langle\sigma v\rangle_1^0$, where the superscript 0 indicates the cross section without taking the Sommerfeld enhancement into account. Using $S \simeq 93$, we find that the model point (ϵ, g_1, m_χ, M_{V_1}) = (0.01, 0.1, 1500 GeV, 2994.2 GeV) in the parameter space of the KM model can give rise to $\langle\sigma v\rangle_1 = 3.9 \times 10^{-25}\text{cm}^3/\text{s}$ which is needed to fit the DAMPE data.

The DM relic abundance which is primarily determined by the DM annihilation cross section at the so-called freeze-out epoch at the early universe. Typical freeze-out occurs at the temperature $T \simeq m_\chi/(20-25)$ such that the DM velocity is approximately $v \simeq 1/4$, where DM annihilation cross section no longer receives significant Sommerfeld enhancement that is present at the current galaxy. We compute the DM annihilation cross section for the processes $\chi\bar{\chi} \to V_1 \to f\bar{f}$ (KM) and $\chi\bar{\chi} \to V_2V_2$ at the freeze-out and find that $\langle\sigma v\rangle_1 = 1.0 \times 10^{-28}\,\text{cm}^3/\text{s}$, and $\langle\sigma v\rangle_2 = 2.2 \times 10^{-26}\,\text{cm}^3/\text{s}$, when $T = m_\chi/25$. Thus the total DM annihilation cross section is approximately $2.2 \times 10^{-26}\,\text{cm}^3/\text{s}$ at freeze-out which is very close to the canonical thermal DM annihilation cross section needed to generate the right DM relic density in the universe. We note that there is a three orders of magnitude boost on $\langle\sigma v\rangle_1$ at current galaxy relative to the early universe, owing to both the Breit-Wigner enhancement and the Sommerfeld enhancement in this annihilation channel.

JHEP06(2019)109

11 Conclusions

There are two exotic features present in the new cosmic electron spectrum observed by the DAMPE collaboration, including a break at 0.9 TeV and a peak at 1.4 TeV. We propose to simultaneously explain both features in the DAMPE data via annihilations from one DM species that interacts with SM via two different mediators. Thus two different DM annihilations channels via the two mediators generate the two new features in the cosmic electron energy spectrum near TeV. The annihilation process mediated by the heavier V_1 boson generates the 1.4 TeV peak; the annihilation process mediated by the lighter V_2 boson produces the extended break near 0.9 TeV.

In this work, we consider two concrete examples of the two-mediator DM models. In both cases the lighter V_2 boson is $L_\mu - L_\tau$ gauged and has mass 10 GeV such that V_2 can be on-shell produced in annihilations of DM which is taken to be 1.5 TeV. We consider the heavier V_1 boson to be either electrophilic or kinetically mixed with the SM hypercharge.

We assume a single power-law cosmic electron background which contains only two parameters and a DM subhalo which is 0.3 kpc from us. Both electrophilic and KM V_1 bosons provide good fits to the 1.4 TeV excess, with the annihilation cross section $4.9 \times 10^{-26}\,\mathrm{cm}^3/\mathrm{s}$ and $3.9 \times 10^{-25}\,\mathrm{cm}^3/\mathrm{s}$ respectively; the $L_\mu - L_\tau$ gauge boson V_2 provides a good fit to the break with the annihilation cross section $2.0 \times 10^{-24}\,\mathrm{cm}^3/\mathrm{s}$.

Several experimental constraints on the DM models are analyzed, including HESS, Fermi IGBG, AMS positron fraction and LHC dilepton searches. Gamma rays expected at the HESS search region are mainly coming from annihilations via the V_2 boson due to the larger cross section. HESS constraints are very sensitive to the DM density profile for the MW halo. The needed cross section for the V_2 process is excluded if one assumes the NFW or Einasto profile for the MW halo, but still allowed if the isothermal profile is considered. In addition, a substantial amount of gamma rays also arise in DM annihilations via the kinetic-mixing V_1 boson; we find that the gamma rays from both annihilation channels are consistent with HESS data assuming the isothermal profile for the MW halo. We also find that the subhalo cannot be put at the Galactic center direction since it would contribute a significant amount of gamma rays to the HESS search region. Fermi isotropic gamma ray background constraints are sensitive to the distance between the subhalo and us. We find that our models do not violate the Fermi isotropic gamma ray background if the subhalo is placed at 0.3 kpc from us. We also note that one can begin to probe our model with more data accumulated at Fermi. DM annihilations in our model cannot provide satisfactory explanations to the AMS positron fraction excess. Nonetheless, one can use the AMS data to put the constraints on DM models by demanding that the predicted positron fraction in DM models not exceed the AMS measurement. We find that the highest energy bin in the AMS data gives the most stringent bound on the $L_\mu - L_\tau$ gauge boson process, and will probe our model in the near future. We also compute the antiproton flux in our model which is found to be consistent with current AMS data. LHC constraints on the KM V_1 boson are analyzed in the dilepton channel. For a 3 TeV V_1 boson, the upper bound on ϵ is about 0.1.

The DM annihilation cross sections needed to fit DAMPE data are much larger than the canonical thermal cross section. This discrepancy can be nicely explained by the

JHEP06(2019)109

Sommerfeld enhancement due to the light V_2 mediator in the models. Taking into account the non-perturbative Sommerfeld enhancement corrections present in the current galaxy, our model is consistent with the relic density requirement in the thermal DM framework.

Acknowledgments

We thank Farinaldo Queiroz, Yue-Lin Sming Tsai, Yilun Xue, Qiang Yuan, and Lei Zhang for helpful correspondence or discussions. The work is supported in part by the National Natural Science Foundation of China under Grant Nos. 11775109 and U1738134, by the National Recruitment Program for Young Professionals, by the Nanjing University Grant 14902303, by the National Postdoctoral Program for Innovative Talents under Grant No. BX201700116, and by the Jiangsu Planned Projects for Postdoctoral Research Funds under Grant No. 1701130B.

A HESS J-factors

Here we compute the HESS J-factor for different DM profiles. The HESS signal region is a circular region of 1° radius excluding a ±0.3° band in Galactic latitudes [59]. We consider three different DM density profiles (NFW, Einasto, and Isothermal) which have been used in HESS analysis. The NFW profile is given by

$$\rho_{\rm NFW}(r) = \frac{\rho_s}{(r/r_s)(1+r/r_s)^2}, \tag{A.1}$$

where we use $r_s = 21\,\text{kpc}$ [68]. The Einasto profile is given by

$$\rho_{\rm E}(r) = \rho_s \exp\left[-\frac{2}{\alpha}\left(\left(\frac{r}{r_s}\right)^{\alpha} - 1\right)\right], \tag{A.2}$$

where we use $\alpha = 0.17$ and $r_s = 20\,\text{kpc}$ [68]. The isothermal profile is given by

$$\rho_{\rm iso}(r) = \frac{\rho_s}{(r/R)^{\gamma}(1+(r/R)^{\alpha})^{(\beta-\gamma)/\alpha}}, \tag{A.3}$$

where we use $R = 3.5\,\text{kpc}$, $\alpha = 2$, $\beta = 2$ and $\gamma = 0$ [69]. The value of ρ_s in all the above profiles are chosen such that the local DM density is normalized to $\rho_\chi(8.5\text{ kpc}) = 0.39\,\text{GeV/cm}^3$. We compute the HESS J-factors for these DM profiles using eq. (6.2)

$$\begin{aligned} J_{\rm NFW} &= 2.25\times10^{21}\ \text{GeV}^2/\text{cm}^5, \\ J_{\rm E} &= 4.41\times10^{21}\ \text{GeV}^2/\text{cm}^5, \\ J_{\rm iso} &= 7.23\times10^{19}\ \text{GeV}^2/\text{cm}^5. \end{aligned} \tag{A.4}$$

HESS collaboration [59] provides the J-factors for two profiles: $J_{\rm NFW} = 2.67\times10^{21}\ \text{GeV}^2/\text{cm}^5$ and $J_{\rm E} = 4.92\times10^{21}\ \text{GeV}^2/\text{cm}^5$. Thus our calculation here yields slightly smaller J-factors than HESS. We use the $J_{\rm NFW}$ and $J_{\rm E}$ values provided by HESS [59] in the rescaling method to be described in appendix B. Because the J-factor for the isothermal profile is not given explicitly by HESS [59], we use our calculated $J_{\rm iso}$ value in the analysis.

JHEP06(2019)109

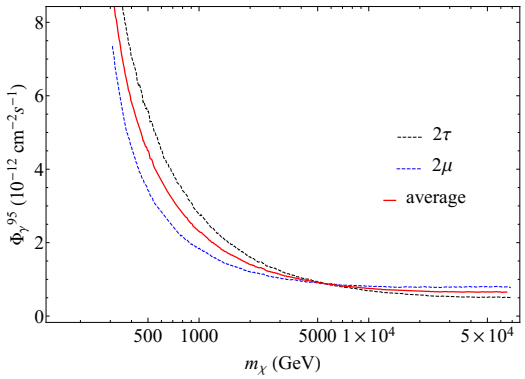

Figure 16. HESS 95% CL upper bound on the total gamma ray flux Φ_γ^{95} in the energy range $160\,\text{GeV} < E_\gamma < m_\chi$ [59]. The 2μ (2τ) curve is obtained based on the HESS upper bound on the annihilation cross section curve in the $\chi\bar{\chi} \to \mu^+\mu^-$ ($\chi\bar{\chi} \to \tau^+\tau^-$) channel [59]. The "average" curve is the arithmetic mean of the 2μ and 2τ curves.

B Rescaling method for HESS limits

Here we describe the "rescaling" method used in our analysis to obtain the HESS limits. We first digitize the 95% CL upper bound on DM annihilation cross section $\langle\sigma v\rangle^{95}(m_\chi)$ from the HESS 254-h data analysis [59] for one specific annihilation channel, for instance the $\chi\bar{\chi} \to \mu^+\mu^-$ annihilation channel. The 95% CL upper bound on the total gamma ray flux $\Phi_\gamma^{95}(m_\chi)$ can be obtained by integrating the differential flux given in eq. (6.1) over the gamma ray energy range $160\,\text{GeV} < E_\gamma < m_\chi$, where we used the Einasto J-factor J_E given in ref. [59]. The HESS constraints can then be calculated for different DM annihilation channels by integrating the differential flux given in eq. (6.1) taking into account different halo profiles and different gamma ray energy spectra. Figure 16 shows the HESS 95% CL bound on $\Phi_\gamma^{95}(m_\chi)$ for the $\chi\bar{\chi} \to \mu^+\mu^-$ and $\chi\bar{\chi} \to \tau^+\tau^-$ annihilation channels. For the on-shell produced vector bosons in the $L_\mu - L_\tau$ model, we use the average value of $\Phi_\gamma^{95}(m_\chi)$ of the $\chi\bar{\chi} \to \mu^+\mu^-$ and $\chi\bar{\chi} \to \tau^+\tau^-$ annihilation channels to compute the HESS limits.

C Green's function method for antiproton flux

We use the Green's function method to compute the antiproton flux arising from DM annihilations in a nearby subhalo. The antiproton flux is given by [70]

$$\Phi^{\chi-\text{SH}}(\mathbf{x}, T) = \frac{v_{\bar{p}}}{4\pi} \int d^3x_s\, G(\mathbf{x}, \mathbf{x}_s, T) Q(\mathbf{x}_s, T), \tag{C.1}$$

where the subscript s denotes the source, T is the kinetic energy of antiproton, $G(\mathbf{x}, \mathbf{x}_s, T)$ is the Green's function, $v_{\bar{p}}$ is the antiproton velocity, $\Phi^{\chi-\text{SH}}(\mathbf{x}, T)$ is the antiproton flux due to DM annihilations in the subhalo, which has the unit of (GeV^{-1} m^{-2} s^{-1} sr^{-1}), and $Q(\mathbf{x}_s, T)$ is the source term due to DM annihilation, which can be computed via

$$Q(\mathbf{x_s}, T) = \frac{1}{4} \frac{\rho_\chi^2(\mathbf{x_s})}{m_\chi^2} \langle\sigma v\rangle \frac{dN}{dT}(T), \tag{C.2}$$

JHEP06(2019)109

where m_χ is the DM mass, $\rho_\chi(\mathbf{x_s})$ is the DM mass density, $\langle\sigma v\rangle$ is the velocity-averaged DM annihilation cross section, dN/dT is the antiproton energy spectrum per DM annihilation. Here we do not take into account the antiproton energy loss since it is negligible at the scale of interest. The Green's function for the antiproton flux can be obtained via [70, 71]

$$G(\mathbf{x}, \mathbf{x}_s, T) = \frac{\exp(-k_v|z|)}{2\pi KL} \sum_{n=0}^{\infty} c_n^{-1} K_0(r\sqrt{k_n^2 + k_v^2}) \sin[k_n L] \sin[k_n(L - |z|)] \tag{C.3}$$

where the K_0 function is modified Bessel function of the second kind, r and z are the differences in the cylindrical coordinates between source and Earth, $k_v = V_c/(2K)$, $c_n = 1 - \sin 2\omega_n/(2\omega_n)$ with $\omega_n \equiv k_n L$, and the quantity k_n is the solution of $\omega_n \cot \omega_n + (h\Gamma_{\rm ann}/K + k_v)L = 0$. We adopt the 'med' profile for the propagation [50] in which $L = 4\,\mathrm{kpc}$, $K = K_0\beta(p/\mathrm{GeV})^\delta$, where $p = \sqrt{T^2 + 2m_p T}$ is the antiproton momentum, $\beta = v_{\bar{p}}/c$, $\delta = 0.7$, and $K_0 = 0.0112\,\mathrm{kpc}^2/\mathrm{Myr}$. For the convective wind, we use $V_c = 12\,\mathrm{km/s}$. We use $h = 0.1\,\mathrm{kpc}$ [50] as the thickness of interstellar protons in the galactic plane. We use $\Gamma_{\rm ann} = (n_H + 4^{2/3} n_{\rm He})\sigma_{p\bar{p}}^{\rm ann} v_{\bar{p}}$ to compute the annihilate rate between antiproton with interstellar protons in the galactic plane, where we use $n_H = 1/\mathrm{cm}^3$ and $n_{\rm He} = 0.07\, n_H$ [50]. The annihilation cross section $\sigma_{p\bar{p}}^{\rm ann}$ is given by [50, 72, 73]

$$\sigma_{p\bar{p}}^{\rm ann} = \begin{cases} 661(1 + 0.0115T^{-0.774} - 0.984T^{0.0151})\ \mathrm{mbarn}, & \text{for } T < 15.5\,\mathrm{GeV}; \\ 36T^{-0.5}\ \mathrm{mbarn}, & \text{for } T \geq 15.5\,\mathrm{GeV}. \end{cases} \tag{C.4}$$

References

[1] DAMPE collaboration, *Direct detection of a break in the teraelectronvolt cosmic-ray spectrum of electrons and positrons*, *Nature* **552** (2017) 63 [arXiv:1711.10981] [INSPIRE].

[2] K. Fang, X.-J. Bi and P.-F. Yin, *Explanation of the knee-like feature in the DAMPE cosmic $e^- + e^+$ energy spectrum*, *Astrophys. J.* **854** (2018) 57 [arXiv:1711.10996] [INSPIRE].

[3] I. Cholis, T. Karwal and M. Kamionkowski, *Features in the Spectrum of Cosmic-Ray Positrons from Pulsars*, *Phys. Rev.* **D 97** (2018) 123011 [arXiv:1712.00011] [INSPIRE].

[4] X.-J. Huang, Y.-L. Wu, W.-H. Zhang and Y.-F. Zhou, *Origins of sharp cosmic-ray electron structures and the DAMPE excess*, *Phys. Rev.* **D 97** (2018) 091701 [arXiv:1712.00005] [INSPIRE].

[5] Q. Yuan et al., *Interpretations of the DAMPE electron data*, arXiv:1711.10989 [INSPIRE].

[6] X. Liu and Z. Liu, *TeV dark matter and the DAMPE electron excess*, *Phys. Rev.* **D 98** (2018) 035025 [arXiv:1711.11579] [INSPIRE].

[7] Y.-Z. Fan, W.-C. Huang, M. Spinrath, Y.-L.S. Tsai and Q. Yuan, *A model explaining neutrino masses and the DAMPE cosmic ray electron excess*, *Phys. Lett.* **B 781** (2018) 83 [arXiv:1711.10995] [INSPIRE].

JHEP06(2019)109

[8] G.H. Duan, L. Feng, F. Wang, L. Wu, J.M. Yang and R. Zheng, *Simplified TeV leptophilic dark matter in light of DAMPE data*, *JHEP* **02** (2018) 107 [arXiv:1711.11012] [INSPIRE].

[9] P.-H. Gu and X.-G. He, *Electrophilic dark matter with dark photon: from DAMPE to direct detection*, *Phys. Lett.* **B 778** (2018) 292 [arXiv:1711.11000] [INSPIRE].

[10] L. Zu, C. Zhang, L. Feng, Q. Yuan and Y.-Z. Fan, *Constraints on the box-shaped cosmic ray electron feature from dark matter annihilation with the AMS-02 and DAMPE data*, *Phys. Rev.* **D 98** (2018) 063010 [arXiv:1711.11052] [INSPIRE].

[11] Y.-L. Tang, L. Wu, M. Zhang and R. Zheng, *Lepton-portal Dark Matter in Hidden Valley model and the DAMPE recent results*, *Sci. China Phys. Mech. Astron.* **61** (2018) 101003 [arXiv:1711.11058] [INSPIRE].

[12] W. Chao and Q. Yuan, *The electron-flavored Z'-portal dark matter and the DAMPE cosmic ray excess*, arXiv:1711.11182 [INSPIRE].

[13] P. Athron, C. Balázs, A. Fowlie and Y. Zhang, *Model-independent analysis of the DAMPE excess*, *JHEP* **02** (2018) 121 [arXiv:1711.11376] [INSPIRE].

[14] J. Cao, L. Feng, X. Guo, L. Shang, F. Wang and P. Wu, *Scalar dark matter interpretation of the DAMPE data with* U(1) *gauge interactions*, *Phys. Rev.* **D 97** (2018) 095011 [arXiv:1711.11452] [INSPIRE].

[15] G.H. Duan, X.-G. He, L. Wu and J.M. Yang, *Leptophilic dark matter in gauged* $\mathrm{U}(1)_{L_e-L_\mu}$ *model in light of DAMPE cosmic ray* $e^+ + e^-$ *excess*, *Eur. Phys. J.* **C 78** (2018) 323 [arXiv:1711.11563] [INSPIRE].

[16] P.-H. Gu, *Radiative Dirac neutrino mass, DAMPE dark matter and leptogenesis*, arXiv:1711.11333 [INSPIRE].

[17] W. Chao, H.-K. Guo, H.-L. Li and J. Shu, *Electron Flavored Dark Matter*, *Phys. Lett.* **B 782** (2018) 517 [arXiv:1712.00037] [INSPIRE].

[18] C.-H. Chen, C.-W. Chiang and T. Nomura, *Explaining the DAMPE* e^+e^- *excess using the Higgs triplet model with a vector dark matter*, *Phys. Rev.* **D 97** (2018) 061302 [arXiv:1712.00793] [INSPIRE].

[19] T. Li, N. Okada and Q. Shafi, *Scalar dark matter, Type II Seesaw and the DAMPE cosmic ray* $e^+ + e^-$ *excess*, *Phys. Lett.* **B 779** (2018) 130 [arXiv:1712.00869] [INSPIRE].

[20] R. Zhu and Y. Zhang, *Graviton-mediated dark matter model explanation the DAMPE electron excess and search at* e^+e^- *colliders*, arXiv:1712.01143 [INSPIRE].

[21] P.-H. Gu, *Quasi-degenerate dark matter for DAMPE excess and 3.5 keV line*, *Sci. China Phys. Mech. Astron.* **61** (2018) 101005 [arXiv:1712.00922] [INSPIRE].

[22] T. Nomura and H. Okada, *Radiative seesaw models linking to dark matter candidates inspired by the DAMPE excess*, *Phys. Dark Univ.* **21** (2018) 90 [arXiv:1712.00941] [INSPIRE].

[23] K. Ghorbani and P.H. Ghorbani, *DAMPE electron-positron excess in leptophilic Z' model*, *JHEP* **05** (2018) 125 [arXiv:1712.01239] [INSPIRE].

[24] J. Cao et al., *Explaining the DAMPE data with scalar dark matter and gauged* $\mathrm{U}(1)_{L_e-L_\mu}$ *interaction*, *Eur. Phys. J.* **C 78** (2018) 198 [arXiv:1712.01244] [INSPIRE].

[25] J.-S. Niu, T. Li, R. Ding, B. Zhu, H.-F. Xue and Y. Wang, *Bayesian analysis of the break in DAMPE lepton spectra*, *Phys. Rev.* **D 97** (2018) 083012 [arXiv:1712.00372] [INSPIRE].

JHEP06(2019)109

[26] F. Yang, M. Su and Y. Zhao, *Dark Matter Annihilation from Nearby Ultra-compact Micro Halos to Explain the Tentative Excess at* ~ 1.4 *TeV in DAMPE data*, arXiv:1712.01724 [INSPIRE].

[27] R. Ding, Z.-L. Han, L. Feng and B. Zhu, *Confronting the DAMPE Excess with the Scotogenic Type-II Seesaw Model*, *Chin. Phys.* **C 42** (2018) 083104 [arXiv:1712.02021] [INSPIRE].

[28] G.-L. Liu, F. Wang, W. Wang and J.M. Yang, *Explaining DAMPE results by dark matter with hierarchical lepton-specific Yukawa interactions*, *Chin. Phys.* **C 42** (2018) 035101 [arXiv:1712.02381] [INSPIRE].

[29] S.-F. Ge, H.-J. He and Y.-C. Wang, *Flavor Structure of the Cosmic-Ray Electron/Positron Excesses at DAMPE*, *Phys. Lett.* **B 781** (2018) 88 [arXiv:1712.02744] [INSPIRE].

[30] Y. Zhao, K. Fang, M. Su and M.C. Miller, *A strong test of the dark matter origin of a TeV electron excess using IceCube neutrinos*, *JCAP* **06** (2018) 030 [arXiv:1712.03210] [INSPIRE].

[31] Y. Sui and Y. Zhang, *Prospects of type-II seesaw models at future colliders in light of the DAMPE* e^+e^- *excess*, *Phys. Rev.* **D 97** (2018) 095002 [arXiv:1712.03642] [INSPIRE].

[32] N. Okada and O. Seto, *DAMPE excess from decaying right-handed neutrino dark matter*, *Mod. Phys. Lett.* **A 33** (2018) 1850157 [arXiv:1712.03652] [INSPIRE].

[33] J. Cao, X. Guo, L. Shang, F. Wang, P. Wu and L. Zu, *Scalar dark matter explanation of the DAMPE data in the minimal Left-Right symmetric model*, *Phys. Rev.* **D 97** (2018) 063016 [arXiv:1712.05351] [INSPIRE].

[34] Z.-L. Han, W. Wang and R. Ding, *Radiative Seesaw Model and DAMPE Excess from Leptophilic Gauge Symmetry*, *Eur. Phys. J.* **C 78** (2018) 216 [arXiv:1712.05722] [INSPIRE].

[35] J.-S. Niu, T. Li and F.-Z. Xu, *A Simple and Natural Interpretations of the DAMPE Cosmic Ray Electron/Positron Spectrum within Two Sigma Deviations*, *Eur. Phys. J.* **C 79** (2019) 125 [arXiv:1712.09586] [INSPIRE].

[36] T. Nomura, H. Okada and P. Wu, *A radiative neutrino mass model in light of DAMPE excess with hidden gauged* U(1) *symmetry*, *JCAP* **05** (2018) 053 [arXiv:1801.04729] [INSPIRE].

[37] Q. Yuan and L. Feng, *Dark Matter Particle Explorer observations of high-energy cosmic ray electrons plus positrons and their physical implications*, *Sci. China Phys. Mech. Astron.* **61** (2018) 101002 [arXiv:1807.11638] [INSPIRE].

[38] X. Pan, C. Zhang and L. Feng, *Interpretation of the DAMPE 1.4 TeV peak according to the decaying dark matter model*, *Sci. China Phys. Mech. Astron.* **61** (2018) 101006.

[39] B. Wang, X. Bi, S. Lin and P. Yin, *Explanations of the DAMPE high energy electron/positron spectrum in the dark matter annihilation and pulsar scenarios*, *Sci. China Phys. Mech. Astron.* **61** (2018) 101004.

[40] O. Balducci, S. Hofmann and A. Kassiteridis, *Small-scale structure from charged leptophilia*, arXiv:1812.02182 [INSPIRE].

[41] F. Elahi and S. Khatibi, *Multi-Component Dark Matter in a Non-Abelian Dark Sector*, arXiv:1902.04384 [INSPIRE].

[42] A. Fowlie, *DAMPE squib? Significance of the 1.4 TeV DAMPE excess*, *Phys. Lett.* **B 780** (2018) 181 [arXiv:1712.05089] [INSPIRE].

[43] J.F. Navarro, C.S. Frenk and S.D.M. White, *The structure of cold dark matter halos*, *Astrophys. J.* **462** (1996) 563 [astro-ph/9508025] [INSPIRE].

JHEP06(2019)109

[44] H. Zhao, *Analytical models for galactic nuclei*, *Mon. Not. Roy. Astron. Soc.* **278** (1996) 488 [astro-ph/9509122] [INSPIRE].

[45] J.F. Navarro, C.S. Frenk and S.D.M. White, *A universal density profile from hierarchical clustering*, *Astrophys. J.* **490** (1997) 493 [astro-ph/9611107] [INSPIRE].

[46] M. Cirelli et al., *PPPC 4 DM ID: A Poor Particle Physicist Cookbook for Dark Matter Indirect Detection*, *JCAP* **03** (2011) 051 [*Erratum ibid.* **10** (2012) E01] [arXiv:1012.4515] [INSPIRE].

[47] V.L. Ginzburg and S.I. Syrovatskii, *The Origin of Cosmic Rays*, Pergamon, Oxford, (1964).

[48] M. Kuhlen and D. Malyshev, *ATIC, PAMELA, HESS, Fermi and nearby Dark Matter subhalos*, *Phys. Rev.* **D 79** (2009) 123517 [arXiv:0904.3378] [INSPIRE].

[49] T. Delahaye, J. Lavalle, R. Lineros, F. Donato and N. Fornengo, *Galactic electrons and positrons at the Earth:new estimate of the primary and secondary fluxes*, *Astron. Astrophys.* **524** (2010) A51 [arXiv:1002.1910] [INSPIRE].

[50] M. Cirelli, R. Franceschini and A. Strumia, *Minimal Dark Matter predictions for galactic positrons, anti-protons, photons*, *Nucl. Phys.* **B 800** (2008) 204 [arXiv:0802.3378] [INSPIRE].

[51] J. Mardon, Y. Nomura, D. Stolarski and J. Thaler, *Dark Matter Signals from Cascade Annihilations*, *JCAP* **05** (2009) 016 [arXiv:0901.2926] [INSPIRE].

[52] A. Ibarra, S. Lopez Gehler and M. Pato, *Dark matter constraints from box-shaped gamma-ray features*, *JCAP* **07** (2012) 043 [arXiv:1205.0007] [INSPIRE].

[53] M. Abdullah, A. DiFranzo, A. Rajaraman, T.M.P. Tait, P. Tanedo and A.M. Wijangco, *Hidden on-shell mediators for the Galactic Center γ-ray excess*, *Phys. Rev.* **D 90** (2014) 035004 [arXiv:1404.6528] [INSPIRE].

[54] J.M. Cline, G. Dupuis, Z. Liu and W. Xue, *The windows for kinetically mixed Z'-mediated dark matter and the galactic center gamma ray excess*, *JHEP* **08** (2014) 131 [arXiv:1405.7691] [INSPIRE].

[55] P. Agrawal, B. Batell, P.J. Fox and R. Harnik, *WIMPs at the Galactic Center*, *JCAP* **05** (2015) 011 [arXiv:1411.2592] [INSPIRE].

[56] J.M. Cline, G. Dupuis, Z. Liu and W. Xue, *Multimediator models for the galactic center gamma ray excess*, *Phys. Rev.* **D 91** (2015) 115010 [arXiv:1503.08213] [INSPIRE].

[57] D. Feldman, Z. Liu and P. Nath, *PAMELA Positron Excess as a Signal from the Hidden Sector*, *Phys. Rev.* **D 79** (2009) 063509 [arXiv:0810.5762] [INSPIRE].

[58] H.E.S.S. collaboration, *Search for a Dark Matter annihilation signal from the Galactic Center halo with H.E.S.S*, *Phys. Rev. Lett.* **106** (2011) 161301 [arXiv:1103.3266] [INSPIRE].

[59] H.E.S.S. collaboration, *Search for dark matter annihilations towards the inner Galactic halo from 10 years of observations with H.E.S.S*, *Phys. Rev. Lett.* **117** (2016) 111301 [arXiv:1607.08142] [INSPIRE].

[60] S. Profumo, F.S. Queiroz, J. Silk and C. Siqueira, *Searching for Secluded Dark Matter with H.E.S.S., Fermi-LAT and Planck*, *JCAP* **03** (2018) 010 [arXiv:1711.03133] [INSPIRE].

[61] FERMI-LAT collaboration, *The spectrum of isotropic diffuse gamma-ray emission between 100 MeV and 820 GeV*, *Astrophys. J.* **799** (2015) 86 [arXiv:1410.3696] [INSPIRE].

JHEP06(2019)109

[62] AMS collaboration, *High Statistics Measurement of the Positron Fraction in Primary Cosmic Rays of 0.5–500 GeV with the Alpha Magnetic Spectrometer on the International Space Station*, *Phys. Rev. Lett.* **113** (2014) 121101 [INSPIRE].

[63] AMS collaboration, *Antiproton Flux, Antiproton-to-Proton Flux Ratio and Properties of Elementary Particle Fluxes in Primary Cosmic Rays Measured with the Alpha Magnetic Spectrometer on the International Space Station*, *Phys. Rev. Lett.* **117** (2016) 091103 [INSPIRE].

[64] ATLAS collaboration, *Search for new high-mass phenomena in the dilepton final state using* $36\,fb^{-1}$ *of proton-proton collision data at* $\sqrt{s} = 13\,TeV$ *with the ATLAS detector*, *JHEP* **10** (2017) 182 [arXiv:1707.02424] [INSPIRE].

[65] Lei Zhang, private communication.

[66] S. Cassel, *Sommerfeld factor for arbitrary partial wave processes*, *J. Phys.* **G 37** (2010) 105009 [arXiv:0903.5307] [INSPIRE].

[67] T.R. Slatyer, *The Sommerfeld enhancement for dark matter with an excited state*, *JCAP* **02** (2010) 028 [arXiv:0910.5713] [INSPIRE].

[68] L. Pieri, J. Lavalle, G. Bertone and E. Branchini, *Implications of High-Resolution Simulations on Indirect Dark Matter Searches*, *Phys. Rev.* **D 83** (2011) 023518 [arXiv:0908.0195] [INSPIRE].

[69] G. Bertone, D. Hooper and J. Silk, *Particle dark matter: Evidence, candidates and constraints*, *Phys. Rept.* **405** (2005) 279 [hep-ph/0404175] [INSPIRE].

[70] J. Lavalle, Q. Yuan, D. Maurin and X.J. Bi, *Full Calculation of Clumpiness Boost factors for Antimatter Cosmic Rays in the light of Lambda-CDM N-body simulation results. Abandoning hope in clumpiness enhancement?*, *Astron. Astrophys.* **479** (2008) 427 [arXiv:0709.3634] [INSPIRE].

[71] D. Maurin, R. Taillet and C. Combet, *Approximate formulae for exotic GCR anti-protons and anti-deuterons: Fluxes and astrophysical uncertainties*, [astro-ph/0609522] [INSPIRE].

[72] L.C. Tan and L.K. Ng, *Calculation of the equilibrium anti-proton spectrum*, *J. Phys.* **G 9** (1983) 227 [INSPIRE].

[73] J. Hisano, S. Matsumoto, O. Saito and M. Senami, *Heavy wino-like neutralino dark matter annihilation into antiparticles*, *Phys. Rev.* **D 73** (2006) 055004 [hep-ph/0511118] [INSPIRE].

JHEP06(2019)109